Temperature Dependence of the Catalytic Two- versus Four-Electron Reduction of Dioxygen by a Hexanuclear Cobalt Complex

Inés Monte-Pérez,[a,⊥] Subrata Kundu,[a,⊥] Anirban Chandra,[a] Kathryn Elizabeth Craigo,[b] Petko Chernev,[c] Uwe Kuhlmann,[d] Holger Dau,[c] Peter Hildebrandt,[d] Claudio Greco,[e] Casey Van Stappen,[b,f*] Nicolai Lehnert,[b*] Kallol Ray[a*]

[a]Humboldt-Universität zu Berlin, Institut für Chemie, Brook-Taylor-Straße 2, D-12489 Berlin (Germany). [b]Department of Chemistry, The University of Michigan, 930 N. University, Ann Arbor, MI 48109 (USA). [c]Freie Universität Berlin, FB Physik, Arnimallee 14, D-14195-Berlin (Germany); [d]Department of Chemistry, Technische Universität Berlin, Straße des 17. Juni 135, 10623 Berlin (Germany); [e] Department of Earth and Environmental Sciences, University of Milan-Bicocca Piazza della Scienza, 1, 20126 Milan (Italy) [f]Current address: Max-Planck Institute for Chemical Energy Conversion, 34-36 Stiftstraße, 45470 Mülheim an der Ruhr (Germany).

⊥ Equal contribution of the two authors

ABSTRACT: The synthesis and characterization of a hexanuclear cobalt complex **1** involving a non-heme ligand system, L1, supported on a Sn_6O_6 stannoxane core are reported. Complex **1** acts as a unique catalyst for dioxygen reduction, whose selectivity can be changed from a preferential $4e^-/4H^+$ dioxygen-reduction (to water) to a $2e^-/2H^+$ process (to hydrogen peroxide) only by increasing the temperature from -50 °C to 25 °C. A variety of spectroscopic methods (^{119}Sn-NMR, Magnetic circular dichroism (MCD), electron paramagnetic resonance (EPR), SQUID, UV-Vis absorption, and X-ray absorption spectroscopy (XAS)) coupled with advanced theoretical calculations has been applied for the unambiguous assignment of the geometric and electronic structure of **1**. The mechanism of the O_2-reduction reaction has been clarified based on kinetic studies on the overall catalytic reaction as well as each step in the catalytic cycle and by low-temperature detection of intermediates. The O_2-binding to **1** results in the efficient formation of a stable end-on μ-1,2-peroxodicobalt(III) intermediate **2** at -50 °C, followed by a proton-coupled electron-transfer (PCET) reduction to complete the O_2-to-$2H_2O$ catalytic conversion in an overall $4e^-/4H^+$ step. In contrast, at higher temperatures (> 20 °C) the constraints provided by the stannoxane core, makes **2** unstable against a preferential proton-transfer (PT) step, leading to the generation of H_2O_2 by a $2e^-/2H^+$ process. The present study provides deep mechanistic insight into the dioxygen reduction process that should serve as useful and broadly applicable principles for future design of more efficient catalysts in fuel cells.

1. Introduction:

The catalytic four-electron reduction of dioxygen (O_2) to water has tremendous technological significance, particularly in fuel cell applications.[1] For example, in fuel cells, the four-electron reduction of O_2 is catalyzed at the cathode by platinum impregnated in carbon.[2] The high loadings of this precious metal that are required to achieve appreciable reactivity have prompted considerable activity in the development of catalysts based on nonprecious metals.[3] Notably, in biology, the Fe-Cu complex of cytochrome c oxidase catalyzes the reduction of dioxygen during aerobic respiration.[4] Therefore, cheap and readily available transition-metal complexes of Fe, Co, Ni and Cu have the potential to replace the expensive Pt alloys in fuel cells to mediate this reaction. The catalytic two-electron reduction of O_2 to H_2O_2 has also attracted considerable interest as H_2O_2 is regarded as a promising candidate for a sustainable and clean energy carrier.[5] For example, H_2O_2 has significant applications as a highly efficient and environmentally benign oxidant in terms of delignification efficiency and the reduction of negative ecological impacts.

In recent years, several Fe, Co, and Cu based complexes have been reported as catalysts for the chemical and electrochemical reduction of dioxygen.[6] In particular, investigations of the catalytic reduction of O_2 by metal complexes in homogeneous systems (using ferrocene derivatives as one-electron reductants and acids as proton sources) have provided deeper insight into the catalytic mechanisms of the two-electron and four-electron reductions of O_2.[7] Here, temperature-dependent kinetic studies in solution have identified a dinuclear metal−peroxo/hydroper- oxo complex as a key intermediate, whose stability and subse- quent reactivity are found to be the controlling factors in thetwo- vs four-electron reductions of O_2. Accordingly, during copper-mediated dioxygen reduction reactions, Nam, Fuku- zumi, Karlin and coworkers have shown that subtle differences in the ligand architecture[6c] or the strength of the acid used as proton source[6e] can significantly alter the geometric and elec- tronic properties of the Cu(II)-OOH intermediate, such that the selectivity of the system changes from a preferential $4e^-/4H^+$ O_2-reduction to the $2e^-/2H^+$ O_2-reduction.

We have recently reported the synthesis of a novel hexanuclear non-heme ligand system, L1, supported on a stannoxane core (Scheme 1), and the iron(II) complex $\{[L1Fe_6]^{12+}\}$ which performs a rare O-O bond formation reaction - the reverse of dioxygen reduction.[8] Theoretical studies have revealed that a Fe–O–O–Fe species is formed as an intermediate following the O-O bond formation step. This result clearly indicates that the framework of the complex formed by L1 stabilizes the M–O–

O–M structure. Therefore, L1 is also expected to be a suitable ligand for a dioxygen reducing catalyst. Herein we report the synthesis and characterization of the corresponding cobalt complex $\{[L1Co_6]^{12+}\}$ and its unprecedented ability to change the number of electrons in the catalytic reduction of O_2 from two to four by simply changing the reaction temperature. The reasons why the same catalyst can act in either the two- or four-electron reduction of O_2 in the presence of decamethylferrocene (Fc*) as a one-electron reductant and trifluoroacetic acid (TFA) as a proton source are elucidated on the basis of detailed kinetic studies of the overall catalytic reactions as well as individual catalytic steps and the characterization of an end-on μ-1,2-peroxodicobalt(III) intermediate, which is presumably formed during the catalytic cycle. The mechanistic insights obtained in this study should serve as useful and broadly applicable principles for future design of more efficient catalysts for the activation of dioxygen.

Scheme 1. The syntheses and structure of complex 1. Color code: nitrogen-blue; carbon-grey; oxygen-red; cobalt-purple; tin-green; sulfur-yellow; and fluorine-greenish yellow.

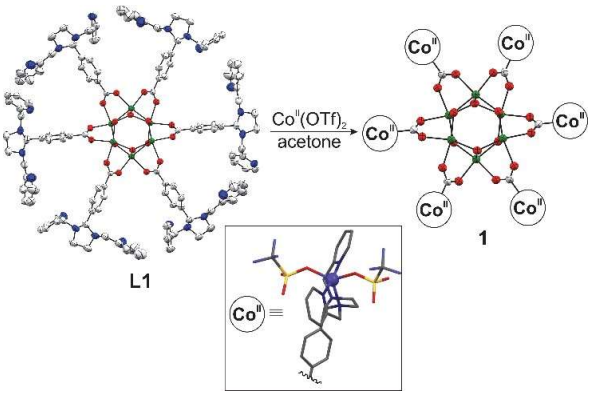

2. Results and Discussion:

2.1. Synthesis and Characterization of $\{[L1Co_6]\}(CF_3SO_2)_{12}$ (1)

Presence of Sn_6O_6 core in 1: The molecular structure of L1 has been reported in our previous communication.[8] It consists of a giant-wheel arrangement of the six non-heme ligand units (involving pyrazole and pyridine N-donors) with a drum-like stannoxane Sn_6O_6 central core serving as the structural support for the hexanucleating assembly. The synthesis of the $\{[L1Co_6]^{12+}\}$ complex was performed following the procedure we reported previously for the $\{[L1Fe_6]^{12+}\}$ complex (Scheme 1). Thus, the reaction of L1 with six eqv. of $Co(OTf)_2$ in acetone yields the metalated species **1** as a yellowish-white powder in 55% yield. The cobalt content of **1**, determined by the inductively coupled plasma mass spectrometry (ICP-MS) method together with the elemental analysis (EA), established the presence of six cobalt atoms per hexameric ligand, with two triflates associated with each cobalt (see SI "synthesis and reactivity studies"). Although ESI-MS and MALDI-TOF experiments to detect the molecular ion peak of **1** were unsuccessful, in the presence of NBu_4CN the MALDI-TOF spectrum of **1** in acetone shows a prominent peak at m/z = 4080.434, whose mass and isotope distribution pattern is consistent with the molecular formula $\{C_{168}H_{180}N_{36}O_{18}Sn_6Co_6Na\}^+$ (M+Na) (Figure S9). The infrared spectrum of **1** depicts a doublet at 1590 and 1607 cm^{-1} for the carboxyl absorption (ν_{COO}), and a strong band at 626 cm^{-1} assigned to $\nu_{Sn\text{-}O}$ for the drum core (Figure S10). The corresponding vibrations for L1 (υ_{COO} at 1590 cm^{-1} and 1605 cm^{-1} and $\upsilon_{Sn\text{-}O}$ at 624 cm^{-1}) are only slightly shifted relative to **1**, which reveals that the S_6 symmetry of the Sn_6O_6 core observed for the molecular structure of L1 is also maintained in **1**. Notably, small alterations in the symmetry of the Sn_6O_6 core were previously shown to result in large shifts of the ν_{COO} and $\nu_{Sn\text{-}O}$ stretches.[9] Furthermore, the ^{119}Sn NMR spectrum (Figure S11) of **1** exhibits a sharp singlet at -485 ppm (for L1 it was observed at -482.4 ppm),[8,9] which is the characteristic signature for a hexameric organostannoxane drum containing a Sn_6O_6 core. Based on the ICP-MS, EA, MALDI-TOF, IR and ^{119}Sn-NMR it can therefore be safely concluded that the reaction of L1 with $Co(OTf)_2$ leads to the metalation of the six metal-binding sites without affecting the structure and symmetry of the drum-like Sn_6O_6 central core.

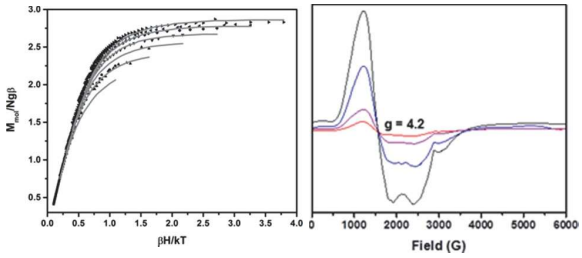

Figure 1. Left: Magnetization data $M_{mol}/Ng\beta$ vs. $\beta H/kT$ for **1** in applied fields ranging from 1 to 7 Tesla. Raw experimental data are presented as black symbols and the scaled best fits are shown as solid gray lines (with the parameters discussed in the text); **Right:** EPR spectra of **1** in CH_2Cl_2 at 8 K at increasing concentrations (red: 1 mM, purple: 3 mM, blue: 6mM and black: 10 mM).

Non-interacting pentacoordinated cobalt(II) centers in 1 involving two bound triflate anions: While efforts to obtain single crystals of **1** were unsuccessful, UV-Visible absorption, EPR, magnetic susceptibility, magnetic circular dichroism(MCD), as well as DFT and *ab initio* studies were performed to establish the coordination environment and electronic structure of the cobalt centers in **1**.

a) Magnetic Susceptibility Measurements: Magnetic measurements of **1** were performed to evaluate whether or not the Co(II) centers interact with one another within the hexanuclear complex. The magnetization data $M_{mol}/Ng\beta$ versus $\beta H/kT$ of **1** was recorded on a Quantum Design MPMS-XL7 SQUID (Superconducting Quantum Interference Device) magnetometer at fields ranging from 1 to 7 Tesla (Figure 1 left), where M_{mol} represents molecular magnetization, N is Avogadro's number, β is the Bohr magneton, H is the magnetic field, k is the Boltzmann constant and T is the absolute temperature. The collected data was modeled using the spin Hamiltonian:

$$\hat{H} = g\beta \boldsymbol{H}\hat{S} + D[\hat{S}_z^2 - S(S+1)/3] + E[\hat{S}_x^2 - \hat{S}_y^2] \qquad (1)$$

where H is the applied magnetic field, g is the g-tensor, S is the electronic spin, and D and E are the axial and rhombic zero field splitting parameters that describe the effects of axial and rhombic ligand fields, respectively. The following magnetic parameters provided the best simulations for the observed magnetization curves: E = 0.5 cm^{-1}, D = 3.5 cm^{-1} (E/D = 0.14) and g_{iso} =

2.23 for a Co(II) S = 3/2 complex. Small amounts of diamagnetic impurity (5%) were also taken into consideration to better fit the magnetization curves. The fits and parameters thus obtained confirm that the cobalt centers of **1** are in an S = 3/2 ground state and suggest that there is negligible interaction between the Co(II) centers within the molecule.

b) EPR Measurements: The X-band EPR spectrum of **1** is presented in Figure 1, right. The observed spectrum appears slightly rhombic, with $g^{\perp} = 4.2$ and $g^{\parallel} \approx 2.1$, which is characteristic of high-spin Co(II).[10] These simulations support an assignment of S = 3/2 for the individual cobalt centers of **1**. The presence of this well-formed S=3/2 signal also implies a lack of interaction between isolated Co(II) sites within the complex. Furthermore, to evaluate the possibility of intermolecular interactions, EPR studies varying the concentration of **1** in CH_2Cl_2 were performed (Figure 1, right). A directly correlated decrease in signal intensity with decreasing concentration is found, supporting the conclusion that no considerable intermolecular interactions occur.

c) Optical studies of 1: With evidence from EPR and magnetic susceptibility measurements that the Co centers of **1** are non-interacting, it was highly interesting to probe the excited states of the complex to gain insight into the electronic structure of the Co(II) centers. Magnetic circular dichroism is a particularly attractive technique as it has the potential to provide information regarding oxidation state, spin state, spin-Hamiltonian parameters, and coordination geometry in addition to resolving electronic transitions.[11] The UV-Vis/NiR absorption and band-deconvoluted MCD spectra are presented in Figure 2 and Table 1.

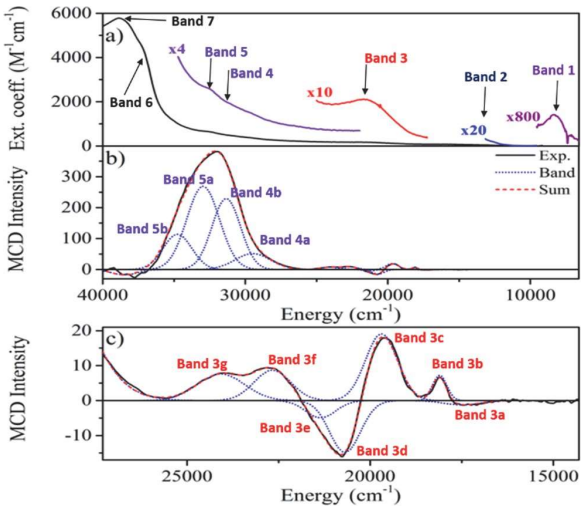

Figure 2. Absorption (a) and MCD spectra (b) of **1**. The expansion of the MCD spectrum in the 29,000-15,000 cm^{-1} range is shown in (c). Absorption spectra were recorded at varying concentrations in dichloromethane. The MCD spectra were acquired at 2 K and 3 T and subjected to a band deconvolution. See Table 1 for the exact energies of the Bands 1-7.

The UV-Vis/NiR absorption of **1** presents a variety of features across a large energy range. At lowest energy, a minute feature at ~8,600 cm^{-1} (Band 1, Figure 2a) appears with an extinction coefficient of ε = ~2 $M^{-1}cm^{-1}$. Next, a weak shoulder (Band 2) appears at ~12,600 cm^{-1} with ε = ~10 $M^{-1}cm^{-1}$. This is followed by a resolved absorption (Band 3) at 21,600 cm^{-1} (ε = ~260 $M^{-1}cm^{-1}$). The remaining spectrum is dominated by a long, sloping absorption background from the stannoxane core with several noticeable shoulders which are not present in the core spectrum (Bands 4-7; Figures 2a and S12). The MCD spectrum of **1**, shown in Figure 2b, is dominated by a large, positive feature ranging from ~27,000-37,000 cm^{-1}, which may be simulated by a minimum of four bands. Lower in energy, a series of weak features (Bands 3a-3g; see also Table 1) appears from ~17,000-25,000 cm^{-1} as highlighted in Figure 2c. All observed features exhibit both temperature- and field-dependence, and therefore must arise through a *C*-term mechanism. Notably, two overlapping bands at 19,690 and 20,690 cm^{-1} (bands 3c and 3d), respectively, form a derivative-shaped signal, corresponding to a pseudo *A*-term. Furthermore, bands 3f and 3g both exhibit a more complex temperature dependence than seen for bands 3b-3e.

Table 1. Summary of the analysis of the absorption and MCD spectra of 1. Absorption spectra were recorded at room temperature (298 K) in dichloromethane. Reported intensities refer to the MCD spectra recorded from a polystyrene film at 2 K and 3 T.

Absorption			MCD			
Band	E (cm^{-1})	ε ($M^{-1}cm^{-1}$)	Band	E (cm^{-1})	Intensity	Sign
1	8,600	2				
2	12,600	10				
			3a	17,490	1.3	-
			3b	18,100	6.7	+
			3c	19,690	18.2	+
3	21,600	260	3d	20,690	14.8	-
			3e	21,350	4.9	-
			3f	22,670	8.7	+
			3g	24,070	7.7	+
4	29,700	380	4a	29,490	51.5	+
			4b	31,340	229	+
5	32,600	650	5a	32,970	268.8	+
			5b	34,770	114	+
6	37,200	4,400				
7	38,900	5,800		38,460	16.5	-

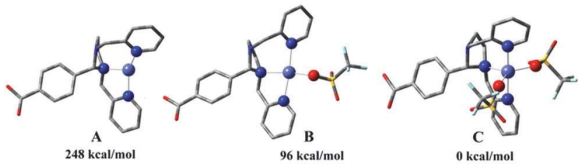

Figure 3. Optimized structural models A, B and C for complex **1**.

d) Computational Studies: To gain further insight into the potential geometric and electronic structure of the Co(II) centers of **1**, a computational study was performed utilizing a simplified

model involving a single arm of the stannoxane core. The use of this model is justified due to the lack of intramolecular interactions between the Co(II) sites (*vide supra*). As triflate was the only counter-anion present during the synthesis, the calculations were also directed to elucidate whether the complex is truly bound by triflate, and if so, by how many. Therefore, model complexes **A**, **B** and **C** were generated, in which zero, one, and two triflates are bound to the Co(II) center, respectively. The optimized molecular structures of **A**, **B** and **C** are shown in Figure 3.

Optimized Structures: Upon optimization, complex **A** adopts a T-shaped geometry, while **B** interestingly forms a square-planar geometry, and **C** shows a more typical trigonal bipyramidal structure (Figure 3). Comparing the calculated free energies of the three models in conjunction with that of free triflate shows that formation of **C** is the most favorable of the three model complexes, with models **B** and **A** being less stable by 96 and 248 kcal/mol, respectively.

TD-DFT Calculations: A comparison of the calculated TD-DFT spectra all three possible compounds (**A**, **B**, and **C**) at the B3LYP/def2-TZVP level[12] for the first 50 roots (utilizing ORCA 3.0)[13] is presented in Figure 4. The Co(II)-centered ligand-field (LF) transitions have been highlighted in red. Models **A** and **C** predict several charge-transfer (CT) states to appear in the 10,000-22,000 cm^{-1} range. In contrast, model **B** remains featureless in this region, which is clearly not in agreement with experiment. However, model **A** predicts a very intense feature at ~30,000 cm^{-1}, which is clearly not in agreement with the experiment. Therefore, model **C** shows the overall best agreement with the experimental data. Nevertheless, while generally informative, it is not possible to indisputably correlate the spectrum of model **C** with the experimentally observed spectrum. It is also difficult to rely upon TD-DFT for an accurate treatment of the ligand-field of metal complexes. Therefore, a series of CASSCF/NEVPT2 calculations [13] were performed for models **A**, **B**, and **C** to predict their ground and excited state properties.

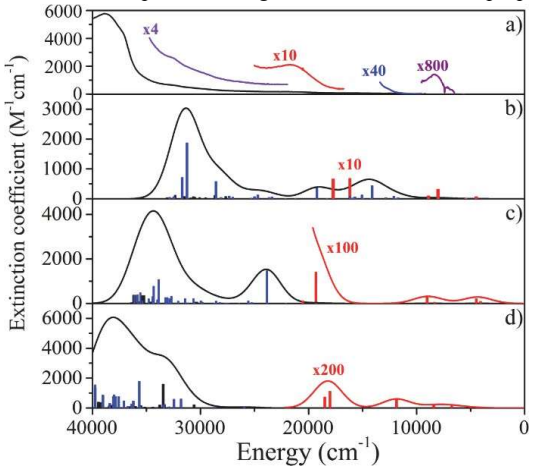

Figure 4. Comparison of the experimentally observed room temperature UV-Vis absorption spectrum of **1** (a), and TD-DFT calculated spectra of structural models **A** (b), **B** (c), and **C** (d). Spectra were generated from the first 50 calculated roots with a Gaussian bandwidth of 3000 cm^{-1}. For b-c, red bars are used to indicate predominately Co(II) centered transitions, while blue bars indicate ligand-to-metal and metal-to-ligand charge transfer transitions. Black bars indicate intra-ligand charge transfer and π-π* transitions of the ligand.

CASSCF/NEVPT2 calculations: Minimal active spaces of seven electrons in five orbitals were selected to describe the predominately Co(II)-centered d-orbitals. Absorption and MCD spectra were calculated for the first 10 quartet and 9 doublet roots of **A**, **B**, and **C** on the basis of the SOC- CASSCF(7,5)/NEVPT2 method as implemented in ORCA 3.0.[13] A summary of the calculated electronic states is providedin Table S1. Due to the effective C_1 symmetry of all three mod- els, states have been grouped together in accordance with the parent state from **O**-symmetry; it is important to note this is onlydone as a formality for book-keeping purposes. Comparing the energies of these transitions, all three models predict major rhombic distortions based upon the drastic splittings of all T- terms. All three models depict the presence of ligand-field based electronic transitions within the range of peaks in the ex- perimental spectrum, assuming an error of ±3,000 cm^{-1}. There- fore, the transition energies themselves do not appear to partic- ularly support one model over the other.

Ligand-field analysis of 1: In a high-spin d^7 system under octahedral symmetry, the ground state corresponds to a $^4T_1$ term, with possible spin-allowed transitions into $^4T_2$, $^4T_1$, and $^4A_2$ excited states. Lowering the symmetry of the system to either D_3 (approximate symmetry of complex **C**) or D_4 (approximate symmetry of complex **B**) results in a splitting of the $^4T_1$ term into ^4E and $^4A_2$, while the $^4T_2$ term splits into ^4E and $^4A_1$ components (Figure S13). In reality, the highly distorted geometries of the three models will result in a further splitting of the ^4E terms. Model **A**, which is of lowest approximate symmetry (C_{2v}), would be expected to represent the extreme of this effect, where the ^4T terms are all reduced to three distinct non-degenerate states. The relative positions of the $^4T_1$, $^4T_2$, and $^4A_2$ terms are highly dependent upon the ligand field, with a crossover point for the $^4T_1$ and $^4A_2$ terms occurring around $\Delta/B = \sim 13$. This, along with the particularly strong influence of the ligand field strength Δ on the relative energy of the $^4A_2$ term, allows for a strong diagnostics of the transition energies for the ligand field parameters of high-spin Co(II) complexes. However, precisely assigning the observed ligand-field transitions is non-trivial since, as mentioned above, each ^4T-term will be split into 2-3 components, depending on the extent of the distortion.

Absorption bands 1-3 (Table 1) all fall within the range of possible LF transitions, with band 3 being further re- solved into six significant features (bands 3b-3g) by MCD. Fig- ure S14 compares the calculated MCD spectra for models **A** – **C** with the experimental data, where **C** shows a slightly better agreement compared to **A**, whereas for model **B** the match with experiment is even poorer. In fact, the assignment of structure**C** to the experimental complex is further supported by the re- sults presented above. Combining the observed experimentalfeatures with insight from the SOC-CASSCF/NEVPT2 calcu- lations of model **C**, we presently propose the following band assignments. First, the 8,600 cm^{-1} band is assigned to a higher energy component of the split $^4T_2$. This is followed by the $^4A_2$ term at 12,600 cm^{-1}. The unusually narrow bandwidth of the positive feature at 18,100 cm^{-1} would typically suggest that thisoptical feature corresponds to either a different state or an alter- native intensity mechanism. However, as this MCD band still exhibits a strong temperature dependence, it is unlikely to arise from a *B*-term mechanism. It is, however, in the expected ener- getic region of the spin-forbidden $^4T_1$ --> $^2T_2$ or $^4T_1$ --> $^2T_1$ tran- sitions. Therefore, and in view of its unusually narrow band- width, it is proposed that the 18,100 cm^{-1} feature arises from a

spin-forbidden transition. The pseudo *A*-term centered at 20,240 cm^{-1} and formed by bands 3c and 3d is assigned as a component of the $^4T_1$ excited state. Naturally, it is difficult to decisively assign the third transition due to the possibility of considerable splitting in this term, and therefore, we simply propose the negative band centered at 21,350 cm^{-1} as the third component of this excited state. The small, higher energy features are assigned as forbidden charge transfer transitions on the basis of their differing field/temperature dependence relative to the assigned LF terms. While not an entirely unique solution, the proposed assignments fit the spectroscopically observed features well. Using these assignments, the ligand field parameters 10Dq and *B* were calculated for models **A**-**C** (and compared with the experiment) using the program AOMX written by H. Adamsky (summarized in Table S2);[14] here again the structure **C** provides the best agreement to the experimental values.

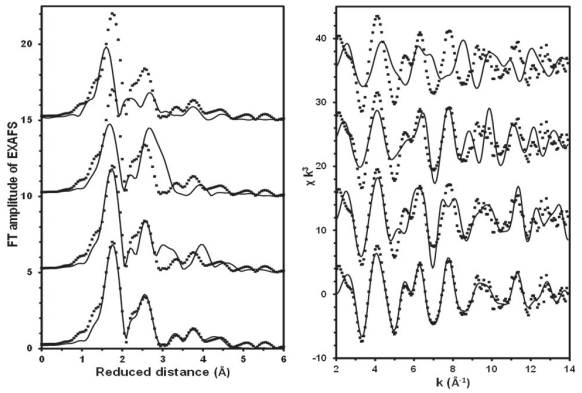

Figure 5. Left: Fourier-transformed k^3-weighted Co *K*-edge EXAFS spectrum of **1.** Experimental data (points) is compared to EXAFS simulations based on the DFT-optimized models (solid lines, from top to bottom) **A**, **B**, **C**, and an EXAFS-optimized version of **C** in which the shell distances were adjusted to optimize the fit to the experimental data; fit details are shown in Table S3. **Right:** The corresponding k^3-weighted EXAFS data in the wavenumber (k) scale prior to the Fourier transformation.

e) X-ray absorption spectroscopy: X-ray absorption spectra at the Co *K*-edge were collected for **1** at 20 K. The experimental extended X-ray absorption fine structure (EXAFS) spectra of **1** were compared to EXAFS simulations based on the DFT structures **A**, **B** and **C** (Figure 5). The comparison of the first peak in the Fourier-transformed EXAFS (at reduced distance ≈ 1.7 Å), corresponding to the first-sphere Co ligands, clearly shows that a three- or four-coordinated Co (**A** and **B**) cannot adequately describe the experimental data. Structure **C**, on the other hand, appears compatible with the experimental EXAFS. Slightly adjusting the Co-ligand distances in structure **C** (bottom trace in Figure 5, Table S3) provides a very good match between simulation and experiment. This analysis, together with the 3/2 ground state, suggests the presence of a penta-coordinated Co(II) center in **1**, similar to that determined previously for the Fe centers[8] of $\{[L1Fe_6]^{12+}\}$ and in agreement with the present MCD and computational results.

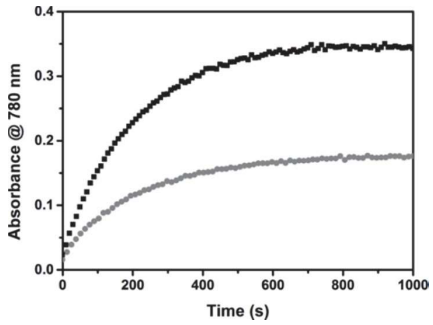

Figure 6. Time profiles of the formation of Fc^{*+} monitored at 780 nm during the reduction of O_2 (0.18 mM) by Fc* (3 mM) and **1** (0.02 mM) in the presence of TFA (10 mM) in acetone at 25 °C (gray circles) as well as at −50 °C (black squares).

2.2. Complex 1 catalyzed dioxygen reduction reactions:

a) Catalytic Two-Electron Reduction of O_2 by Fc* with 1 in the Presence of TFA at 25 °C: The reaction of **1**, Fc*, and TFA with an O_2-saturated acetone solution at 25 °C results in an efficient oxidation of Fc* by O_2 (see SI "Evaluation of the Catalytic activity of **1** towards dioxygen reduction"). The reduction of O_2 was monitored by a rise in absorbance at 780 nm due to decamethylferrocenium (Fc^{*+}) ion (Figure S1). Figure 6 (gray circles) shows the time course of formation of Fc^{*+} in the reduction of O_2 (0.18 mM) by a large excess of Fc* (3 mM) in the presence of **1** (0.02 mM) and TFA (10 mM). The concentration of Fc^{*+} (0.34 mM) formed in the complex **1**-catalyzed reduction of O_2 by Fc* is approximately twice that of the O_2 concentration (0.18 mM). Thus, only two-electron reduction of O_2 occurs at 25 °C and no further reduction occurs to produce more than 2 equiv of Fc^{*+}.

$$O_2 + 2\ Fc^* + 2\ H^+ \rightarrow 2\ Fc^{*+} + H_2O_2 \qquad (2)$$

It was confirmed that H_2O_2 (0.14 mM) is formed in the two-electron reduction of O_2 by iodometric measurements (Figure S2). The slightly lower than expected (0.18 mM) yield of H_2O_2 can be presumably attributed to the competing reaction involving the direct reduction of H_2O_2 with Fc* at 25 °C.[15] The rate of formation of Fc^{*+} obeyed pseudo-first-order kinetics under the conditions that [**1**] ≪ [Fc*] < [TFA]. The pseudo-first-order rate constant (k_{obs}) increased linearly with an increasing concentration of **1** (Figure 7a). The k_{obs} values were also proportional to concentrations of TFA (Figure 7d) and O_2 (Figure 7c). Thus, the kinetics is given by eqs 3 and 4, where k_{cat} is the apparent fourth-order rate constant for the catalytic two-electron reduction of O_2 by Fc* when k_{obs} is given by eq 4.

$$d[Fc^{*+}]/dt = k_{obs}[Fc^*] \qquad (3)$$

$$k_{obs} = k_{cat}[\mathbf{1}][O_2][TFA] \qquad (4)$$

Consistent with this rate equation, the rate of formation of Fc^{*+} also obeyed pseudo-first order kinetics and the observed pseudo-first-order rate constant (k_{obs}) increased linearly with increasing concentration of Fc* (Figure 7b). Notably, the $2e^-$ O_2 reduction by **1**, where the rate is proportional to concentrations not only of **1** but also O_2, TFA, and Fc*, is in sharp contrast to the previously reported case of Co-catalysed [6b] O_2 reduction in which the rate was reported to be rather independent of O_2.

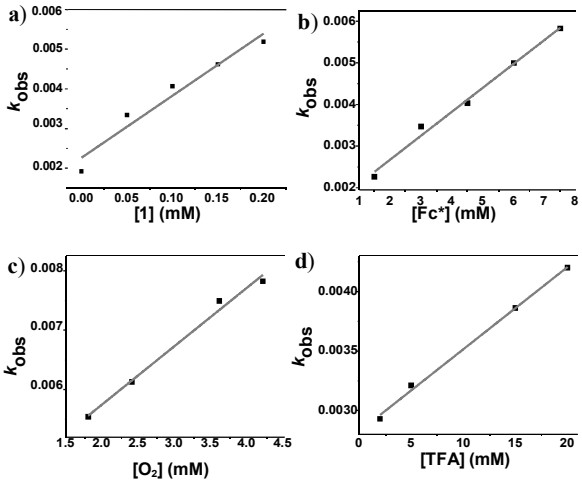

Figure 7. Studies on the two electron reduction of O_2 in acetone at 25 °C catalyzed by **1**. a) k_{obs} vs [**1**] for the O_2-reduction in O_2-saturated acetone (11 mM) with Fc* (3 mM) catalyzed by **1** (0.05-0.2 mM) with TFA (10 mM). b) k_{obs} vs [Fc*] for the O_2-reduction in O_2-saturated acetone with Fc* (1.5-7.5 mM) catalyzed by **1** (0.1 mM) with TFA (10 mM). c) Plot of k_{obs} vs [O_2] for the reduction of O_2 (1.8-4.2 mM) with Fc* (3 mM) catalyzed by **1** (0.1 mM) with TFA (10 mM). d) Plot of k_{obs} vs TFA concentration for the O_2-reduction in O_2-saturated acetone with Fc* (3 mM) catalyzed by **1** (0.1 mM) with TFA (2-20 mM).

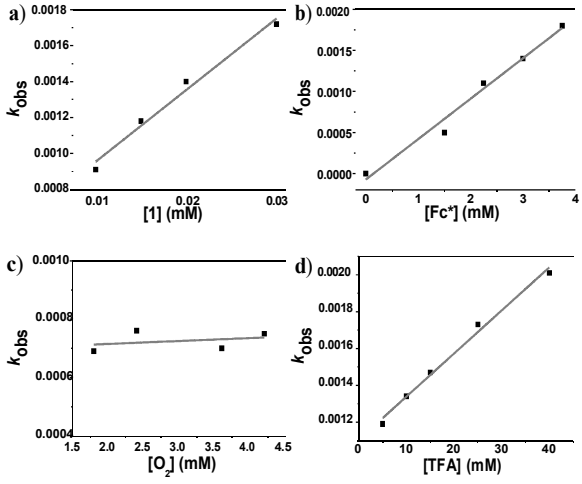

Figure 8: Studies of the four electron reduction of O_2 in acetone at −50 °C catalyzed by **1**. a) k_{obs} vs [**1**] for the reduction of O_2 (11 mM) with Fc* (3 mM) catalyzed by **1** (0.01-0.03 mM) with TFA (10 mM). b) k_{obs} vs [Fc*] for the reduction of O_2 (11 mM) with Fc* (1.5-4 mM) catalyzed by **1** (0.02 mM) with TFA (10 mM). c) Plot of k_{obs} vs [O_2] concentration for the reduction of O_2 (1.75-4.25 mM) with Fc* (3 mM) catalyzed by **1** (0.02 mM) with TFA (10 mM). d) Plot of k_{obs} vs [TFA] for the reduction of O_2 (11 mM) with Fc* (3 mM) catalyzed by **1** (0.02 mM) with TFA (5-40 mM).

b) Catalytic Four-Electron Reduction of O_2 by Fc* with 1 in the Presence of TFA at -50 ºC : Interestingly, when an oxygen-free acetone solution of Fc* (3 mM), TFA (10 mM) and **1** (0.02 mM) was cooled down to −50 °C, the reaction with O_2 (0.18 mM) displayed a different behavior (Figure 6, black squares). Here, the amount of Fc^{*+} generated during the O_2 catalytic reduction was 0.67 mM, which represents 3.74 equivalents relative to the initial concentration of O_2 (0.18 mM). This clearly indicated that at −50 °C a four-electron reduction takes place according to eq 5.

$$O_2 + 4\,Fc^* + 2\,H^+ \rightarrow 4\,Fc^{*+} + H_2O \qquad (5)$$

Iodometric titrations confirmed that no H_2O_2 was formed after the reaction was complete. Furthermore, the time profile in Figure 6 indicates that this process proceeds via a single step rather than by stepwise reduction of O_2 to H_2O_2 and then to H_2O. The formation of Fc^{*+} at −50 ºC also obeyed a pseudo-first-order kinetics. The pseudo-first-order rate constant (k_{obs}'') increased linearly with increasing concentrations of **1** (Figure 8a), Fc* (Figure 8b), and TFA (Figure 8d) but, in contrast to the results at 25º C, did not depend on the O_2 concentration (Figure 8c). Thus, the kinetic equation at −50 ºC is

$$d[Fc^{*+}]/dt = k_{obs}''[Fc^*] \qquad (6)$$

$$k_{obs}'' = k_{cat}''[\mathbf{1}][TFA] \qquad (7)$$

where k_{cat}'' is the third-order rate constant for the catalytic 4e−-reduction of O_2 by Fc* at −50 ºC. Notably, a turnover number (TON) of 65 during a lapse of 2000 seconds was determined for the catalyst **1** in the reduction of O_2 to H_2O in acetone at −50 °C. This is in contrast to the TON of 16 determined for **1** in the reduction of O_2 to H_2O_2 in acetone at 25 °C. Thus, **1** is a more efficient catalyst for the four-electron reduction of O_2 to H_2O at -50 ºC than for the two-electron reduction process at 25 ºC.

2.3 Formation, characterization and Reactivity of a Cobalt-peroxide intermediate {[L1Co$_6$(O$_2$)$_3$]}(CF$_3$SO$_2$)$_{12}$(2)

Temperature dependent formation kinetics of 2: In order to elucidate a catalytic mechanism to explain such a unique temperature controlled switch between the $4e^-/4H^+$ and $2e^-/2H^+$ O_2 reduction processes, we examined the reaction of **1** with O_2 (in the absence of TFA and Fc*) to detect any cobalt−dioxygen intermediate. An acetone solution of **1**, when treated with O_2 saturated acetone at −50 °C, results in the formation of an orange species **2** with an intense absorption maximum λ_{max} (ε_{max}, $M^{-1}cm^{-1}$) centered at 470 nm (28,000) (Figure 9 Left). Notably, the 470 nm band resembles the absorption features of the previously reported end-on μ-1,2-peroxo-dicobalt(III) complexes,[16] which are all characterized by the presence of an intense absorption band around 300 - 500 nm with molar extinction coefficients (ε) > 5000 $M^{-1}cm^{-1}$; the alternative side-on-Co(III) peroxo complexes display absorption features with much lower molar extinction coefficients (ε) < 1000 $M^{-1}cm^{-1}$.[17] Generation of **2** is found to be complete within 300 s following first-order kinetics with a rate constant (k_{obs}) of 4.5 x 10^{-4} s^{-1} at −50 ºC (Figure S15). The rate of the reaction is found to be independent of the starting concentration of **1** (0.2 – 1.2 mM), thereby suggesting an intramolecular mechanism (Figure 9, right). Spectrophotometric O_2 titration experiments indicate that the complete conversion of **1** to **2** requires 2.5−3 equiv of O_2 per hexacobalt unit (addition of more than 3 equiv of O_2 does not lead to a further increase of the 470 nm band, shown in Figure 9 left inset). As the temperature is increased, the absorption band at 470 nm due to **2** is decreased; at 25 ºC the intensity of the 470 nm band is approximately 35% of that at −50 ºC (Figure 10). This pro- cess is reversible in the temperature range −50 ºC to +25 ºC. Thus, in contrast to the high-yield formation of **2** at −50 ºC ,

binding of dioxygen to **1** is not favored at +25 °C and the equilibrium lies in the direction of **1**.

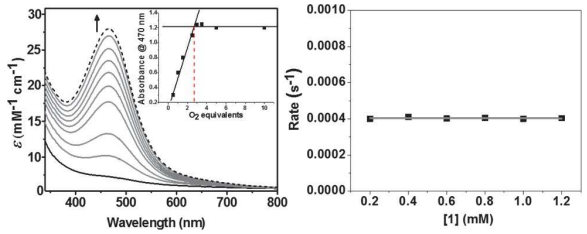

Figure 9: Left: Absorption spectra of **1** (solid trace) and **2** (dashed trace) in acetone at −50 °C. The intermediate spectra show the conversion of **1** to **2** upon addition of dioxygen gas. Inset: Plot of absorbance at 470 nm vs the equivalents of O_2 used in the reaction. Right: Concentration-independent rate constant for the conversion of **1** to **2** at −50 °C in acetone.

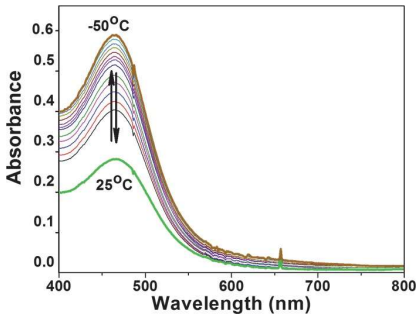

Figure 10: Absorption spectra showing the reversibility of dioxygen binding to **1**. Bubbling O_2 into an acetone solution of **1** (0.02 mM) produces **2** (in high yield) at −50 °C (brown, solid line). Increasing the temperature up to 25 °C produces the green solid spectrum. After re-cooling to −50 °C the brown solid spectrum can be regenerated.

Determination of the electronic and geometric structures of 2: Complex **2** is expected to have an *S*=0 ground state based upon the absence of any signal in the EPR or MCD spectra (Figure S16). The resonance Raman (rR) spectrum (Figure 11A) of **2** in d_6-acetone displays two isotopically sensitive vibrational bands at 868 and 611 cm^{-1} which are downshifted to 819 and 584 cm^{-1}, respectively, in $^{18}O_2$ prepared samples. The 868 cm^{-1} band with an isotopic shift of 49 cm^{-1} (calculated shift $^{16/18}\Delta_{calc.} = 50$ cm^{-1}) is assigned to the O-O stretching mode of a peroxo ligand, and the 611 cm^{-1} band ($^{16/18}\Delta_{exp.} = 27$ cm^{-1}, $^{16/18}\Delta_{calc.} = 28$ cm^{-1}) is consistent with a Co-O stretching mode. In order to probe the oxidation state of cobalt in **2**, X-ray absorption spectroscopic studies at the Co *K*-edge are performed. Figure 11B depicts a comparison of the normalized Co *K*-edge XAS spectra of the oxidized complex **2** with its Co(II) precursor complex **1**. Upon moving from **1** to **2**, the pre-edge peak shifts from 7710.3 eV to 7711.7 eV (Figure 11B inset), thus indicating an increase in the ligand field strength in **2**. A blue shift of *ca.* 1.6 eV in edge energy from **1** (7720.4 eV) to **2** (7722.0 eV) is in agreement with the higher oxidation state of cobalt in **2** (Co^{3+}) relative to **1** (Co^{2+}). The EXAFS data are consistent with a five-coordinate site in **2** with four short Co–N/O bond lengths averaging 1.93 Å and one long Co–N/O bond length of 2.14 Å (Table S3).

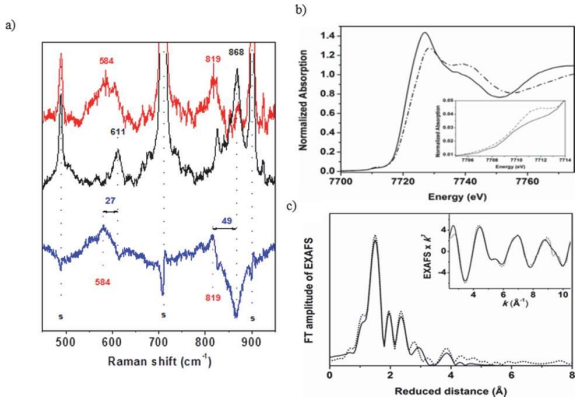

Figure 11: a) Resonance Raman spectra of **2-^{18}O** (red trace), **2-^{16}O** (black trace), and difference [**(2-^{18}O) - (2-^{16}O)**] spectra (blue trace) with 458 nm laser excitation in d_6-Acetone at −80 °C. Solvent bands are marked by "s". **b)** Comparison of normalized Co *K*-edge near edge X-ray absorption spectrum of **1** (solid trace) and **2** (dash-dotted trace). Inset shows the expansion of the pre-edge region. **c)** Fourier-transformed Co *K*-edge EXAFS spectra of **2** [Experimental data: dotted line, Simulation: solid line]. Insets are showing the EXAFS data in wave-vector scale before Fourier transformation.

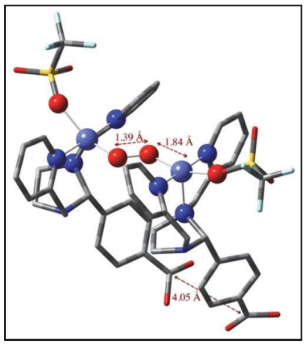

Figure 12: DFT Optimized structure of **2**. The distance between the two carbonyl carbons is fixed at 4.045 Å, with all other atoms allowed to relax during optimization.

The X-ray structure of L1 previously revealed a distance of > 4 Å between the two adjacent metal-binding sites of L1. DFT calculations were therefore performed to assess the viability of forming an intramolecularly bridged peroxo-dicobalt(III) complex in L1. We designed a simplified system containing two monomeric units, where the distance between the two carbonyl carbons were fixed to 4.045 Å, based on the struc- ture of L1,[8] in order to approximate the constraints provided by the stannoxane core. The optimized structure (Figure 12) re- veals a Co^{III}-O-O-Co^{III} unit with the O-O distance of 1.39 Å and Co-O distances of 1.84 and 1.85 Å, which are characteristic of peroxo complexes. Notably, the Co-O distances are predicted to be slightly shorter than those for either Co-triflate (1.952 Å) or Co-pyridines (1.993 and 1.968 Å) which are again shorter than that of the Co-amine (2.17 Å). Thus, the calculations point to one short, three mid, and one long Co-N/O distance, rather than the four short and one long Co-N/O distances derived from the

EXAFS data. However, the calculated vibrational frequencies with ν(Co-O) at 613 and 619 cm–$^{-1}$, and ν(O-O) at 873 cm^{-1} are in excellent agreement with the experiment (ν(Co-O) and ν(O-O) of 611 and 878 cm^{-1}, respectively (Figure 11a). Furthermore, single-point calculations on the optimized geometry favor an antiferromagnetically coupled state between two S=1 Co^{III} centers with a coupling-constant (*J*) of -181 cm^{-1} using the Noodleman formalism.[18] Based on the spectroscopic and structural characterization, complex **2** is therefore assigned as consisting of μ-1,2-peroxo-dicobalt(III) cores, where the O_2^{2-} units act as intramolecular bridges between the cobalt centers in **1**. The possibility of O_2^{2-} acting as intermolecular bridges between the cobalt centers of two different molecules of **1** can be ruled out based on the non-dependence of the rate of formation of **2** on the concentration of **1** (Figure 9, right) and also based on the O_2-titration experiments (Figure 9, left inset). This intramolecular binding mode is also strongly supported by the observed temperature-dependence of the stability of the Co-peroxide complex. The formation of an intramolecularly bridged μ-1,2-peroxo-dicobalt(III) core imposes significant restraints on the conformational flexibility of the Co-binding arms of stannoxane. Great enough restriction would make this an entropically unfavorable process, and therefore sensibly increasingly favor the dissociation of O_2 with increasing temperature, as observed.

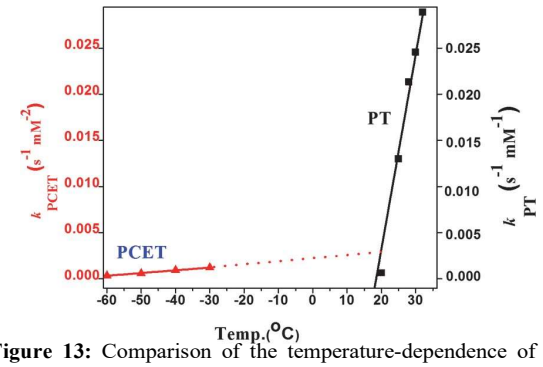

Figure 13: Comparison of the temperature-dependence of the PCET vs PT rate constants for the reduction of **2.**

Reactivity of 2 with Protons and Electrons: The 4e$^-$ reduction of O_2 at –50 °C requires the reduction/protonation of **2** in the presence of Fc* and TFA. Thus, we examined the reduction of **2** by Fc* in both the presence and absence of TFA (and also the protonation of **2** in the presence and absence of Fc*) in deaerated acetone at –50 °C. In the absence of TFA, no reduction of **1** by Fc* was observed. Similarly, in the absence of Fc* no protonation of **2** was observed. A proton coupled electron transfer (PCET) reaction was, however, evident in the presence of both TFA and Fc* (Figure S6), as the absorption band at 470 nm due to **2** disappeared. The reactivity of **2** with Fc* and TFA was also investigated at 25 °C. In the absence of TFA, no reduction of **1** by Fc* was observed, very similar to the findings at –50 °C. However, reaction of **2** with > 12 eqv. of TFA (even in the absence of Fc*) led to the decay of the 470 nm band (Figure S7) and the liberation of H_2O_2 in > 65% yield.

The stability of the μ-1,2-peroxo-dicobalt(III) complex **2** and its ability to undergo reduction by a preferential PCET process at –50 °C and PT at +25 °C offered the opportunity to compare the temperature-dependence of the PCET and PT processes of **2**. It is intuitively clear that this will be the controlling factor in determining the temperature dependence of the 4e$^-$/4H$^+$ *vs* 2e$^-$/2H$^+$ reductions of dioxygen mediated by **1**. PCET rates were determined at –60 °C, –50 °C, –40 °C, and –30 °C under the condition [**2**] ≪ [Fc*] ≪ [TFA] to ensure pseudo first-order kinetics. Notably, at these temperatures the contribution of PT is negligible as evident from the lack of intensity changes of the 470 nm band (corresponding to **2**) in the presence of large excess of TFA only. Similarly, PT rates were determined under the condition [**2**] ≪ [TFA] in the temperaturerange +20 °C to +32 °C, where PCET contributions were not significant. As evident from Figure 13, the variation of PT with the temperature is much more drastic relative to that of PCET, which ensures that at temperatures > + 20 °C PT is the prevailing mechanism for the reduction of **2**. The predominance of PT at higher temperatures originates from the demonstrated insta- bility of the peroxo core in **2** and its tendency to liberate dioxy- gen at +25 °C (Figure 10), which can presumably be attributedto the constraints resulting from the rigid attachment of the metal binding arms to the central stannoxane core of the L1 lig- and via carboxylate bridging.

Scheme 2. Scheme showing the mechanism of the temperature dependent 4e/4H$^+$ vs 2e/2H$^+$ reduction of dioxygen mediated by the dicobalt(II) units of 1

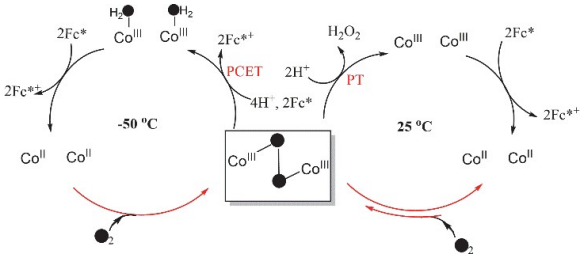

3. Conclusion:

In a previous study we reported the synthesis of a novel hexanucleating non-heme ligand system, L1, supported on a stannoxane core along its iron(II) complex {[L1Fe$_6$]$^{12+}$}, which perfomed a rare O-O bond formation upon reaction with iodosobenzene to yield a superoxo complex, {[L1(Fe^{III}($O_2^{\bullet-}$)Fe^{II})$_3$]$^{12+}$}.[8] The same superoxo species was also formed upon the dioxygen activation reaction by {[L1Fe$_6$]$^{12+}$}. Detailed experimental and theoretical studies confirmed the involvement of an end-on bridged Fe^{III}-O-O-Fe^{III} peroxo species, whose transient nature, however, prevented its isolation even at low temperatures. In the present report we show that the replacement of the iron centers by cobalt leads to a significant increase in the stability of the M-O-O-M core, which allows for the isolation of the {[L1(Co^{III}(O_2)Co^{III})$_3$]}$^{12+}$ complex **2** upon dioxygen activa- tion of the hexanuclear cobalt complex {[L1Co$_6$]$^{12+}$} (**1**) in the temperature range –50 °C to 25 °C. Spectroscopic characterization (together with theoretical studies) of **2** confirms the presence of an antiferromagnetically coupled μ-1,2-peroxodicobalt(III) cores in **2** with an S=0 ground state. Furthermore, the different formation kinetics of **2** at different temperatures is attributable to the constraints imposed by the stannoxane core of L1; at –50 °C the formation of **2** is highly favored (owing to its high enthalpic stability) that leads to the complete oxygenation of **1**. In contrast, an equilibrium binding of O_2 occurs at 25 °C

(due to the entropic instability of **2**), such that only a small portion of **1** is converted to **2**. The differing stability of **2** at −50 °C and 25 °C is also reflected in its reactivity with protons and electrons. Although complex **2** does not undergo protonation or reduction individually at −50 °C, it is capable of undergoing a PCET process in the presence of both TFA and Fc*, leading to the formation of water. In contrast, at 25 °C complex **2** was found to be unstable upon protonatation in the presence of TFA, leading to the liberation of H_2O_2. The stability of the Co^{III}-O_2-Co^{III} core in **2**, together with its temperature-dependent reactivity in the presence of protons and electrons, makes complex **1** a unique catalyst for dioxygen reduction, whose selectivity can be changed from a preferential $4e^-/4H^+$ O_2-reduction to a $2e^-/2H^+$ O_2-reduction by simply increasing the reaction temperature from −50 °C to 25 °C. The overall catalytic cycle is summarized in Scheme 2. The most probable intermediate formed upon dioxygen activation is the $\{[L1(Co^{III}(O_2)Co^{III})_3]\}^{12+}$ species **2**, which is reduced to H_2O by a PCET mechanism at −50 °C, or to H_2O_2 by an uncoupled proton transfer/electron transfer mechanism at 25 °C. In summary, the present study provides deep mechanistic insight into the dioxygen reduction process which should serve as useful and broadly applicable principles for future design of more efficient catalysts in fuel cells.

ASSOCIATED CONTENT

Supporting Information

Materials and methods, synthetic procedures, Figures S1-S16, and Tables S1-S3. This material is available free of charge via the Internet at http://pubs.acs.org.

AUTHOR INFORMATION

Corresponding Authors

kallol.ray@chemie.hu-berlin.de; lehnertn@umich.edu; casey.vanstappen@cec.mpg.de

ACKNOWLEDGMENT

Financial support from the Deutsche Forschungsgemeinschaft (Cluster of Excellence "Unifying Concepts in Catalysis"; EXC 314-2) is gratefully acknowledged. K.R. also thanks the Heisenberg-Program of the Deutsche Forschungsgemeinschaft for financial support. We thank the Helmholtz-Zentrum Berlin for the allocation of synchrotron radiation beamtime.

REFERENCES

(1) (a) Stambouli, A. B.; Traversa, E. *Renewable and Sustainable Energy Rev.* **2002**, *6*, 295. (b) Marković, N. M.; Schmidt, T. J.; Stamenković,V.; Ross, P. N. *Fuel Cells* **2001**, *1*, 105. (c) Steele, B. C. H.; Heinzel, A. *Nature* **2001**, *414*, 345.

(2) Borup, R.; et al. *Chem. Rev.* **2007**, *107*, 3904.

(3) (a) Anson, F. C.; Shi, C.; Steiger, B. *Acc. Chem. Res.* **1997**, *30*, 437. (b) Peljo, P.; Rauhala, T.; Murtomäki, L.; Kallio, T.; Kontturi, K. *Int. J. Hydrogen Energy* **2011**, *36*, 10033. (c) Collman, J. P.; Devaraj, N. K.; Decréau, R. A.; Yang, Y.; Yan, Y.-L.; Ebina, W.; Eberspacher, T. A.; Chidsey, C. E. D. *Science* **2007**, *315*, 1565. (d) Collman, J. P.; Decréau, R. A.; Lin, H.; Hosseini, A.; Yang, Y.; Dey, A.; Eberspacher, T. A. *Proc. Natl. Acad. Sci. U.S.A.* **2009**, *106*, 7320. (e) Collman, J. P.; Ghosh, S.; Dey, A.; Decréau, R. A.; Yang, Y. *J. Am. Chem. Soc.* **2009**, *131*, 5034. (f) Kadish, K. M.; Frémond, L.; Shen, J.; Chen, P.; Ohkubo, K.; Fukuzumi, S.; El Ojaimi, M.; Gros, C. P.; Barbe, J.-M.; Guilard, R. *Inorg. Chem.* **2009**, *48*, 2571. (g) Kadish, K. M.; Shen, J.; Frémond, L.; Chen, P.; Ojaimi, M. E.; Chkounda, M.; Gros, C. P.; Barbe, J.-M.; Ohkubo, K.; Fukuzumi, S.; Guilard, R. *Inorg. Chem.* **2008**, *47*, 6726. (h) Chen, W.; Akhigbe, J.; Brückner, C.; Li, C. M.; Lei, Y. *J. Phys. Chem. C* **2010**, *114*, 8633. (i) Rosenthal, J.; Nocera, D. G. *Acc. Chem. Res.* **2007**, *40*, 543. (j) Dogutan, D. K.; Stoian, S. A.; McGuire, R.; Schwalbe, M.; Teets, T. S.; Nocera, D. G. *J. Am. Chem. Soc.* **2011**, *133*, 131. (k) Teets, T. S.; Cook, T. R.; McCarthy, B. D.; Nocera, D. G. *J. Am. Chem. Soc.* **2011**, *133*, 8114.

(4) (a) Ferguson-Miller, S.; Babcock, G. T. *Chem. Rev.* **1996**, *96*, 2889. (b) Babcock, G. T.; Wikstrom, M. *Nature* **1992**, *356*, 301. (c) Babcock, G. T. *Proc. Natl. Acad. Sci. U.S.A.* **1999**, *96*, 12971. (d) Kaila, V. R. I.; Verkhovsky, M. I.; Wikstrom, M. *Chem. Rev.* **2010**, *110*, 7062.

(5) (a) Yamanaka I.; Murayama T. *Angew. Chem., Int. Ed.* **2008**, *47*, 1900. (b) Disselkamp, R. S. *Int. J. Hydrogen Energy* **2010**, *35*, 1049. (c) Disselkamp, R. S. *Energy Fuels* **2008,** 22, 277. (d) Sanli, A. E.; Aytac, A. *Int. J. Hydrogen Energy* **2011**, *36*, 869. (e) Yamada, Y.; Fukunishi, Y.; Yamazaki, S.; Fukuzumi, S. *Chem. Commun.* **2010,** *46,* 7334. (f) Nishimi, T.; Kamachi, T.; Kato, K.; Kato, T.; Yoshizawa, K. *Eur. J. Org. Chem.* **2011**, *22*, 4113.

(6) (a) Das, D.; Lee, Y.-M.; Ohkubo, K.; Nam, W.; Karlin, K. D.; Fukuzumi, S. *J. Am. Chem. Soc.* **2013**, *135*, 2825. (b) Fukuzumi, S.; Okamoto, K.; Gros, C. P.; Guilard, R. *J. Am. Chem. Soc.* **2004**, *126*, 10441. (c) Fukuzumi, S.; Tahsini, L.; Lee, Y.-M.; Ohkubo, K.; Nam, W.; Karlin, K. D. *J. Am. Chem. Soc.* **2012**, *134*, 7025 (d) Fukuzumi, S.; Mandal, S.; Mase, K.; Ohkubo, K.; Park, H.; Benet-Buchholz, J.; Nam, W.; Llobet, A. *J. Am. Chem. Soc.* **2012**, *134*, 9906. (e) Das, D.; Lee, Y.-M.; Ohkubo, K.; Nam, W.; Karlin, K. D.; Fukuzumi, S. *J. Am. Chem. Soc.* **2013**, *135*, 4018. (f) Thorseth, M. A.; Tornow, C. E.; Tse, E. C. M.; Gewirth, A. A. *Coord. Chem. Rev.* **2013**, *257*, 130. (g) Halime, Z.; Kotani, H.; Li, Y.; Fukuzumi, S.; Karlin, K. D. *Proc. Natl. Acad. Sci. U. S. A.* **2011**, *108*, 13990. (h) Costentin, C.; Dridi, H.; Saveant, J.-M. *J. Am. Chem. Soc.* **2015**, *137*, 13535 (i) Carver, C. T.; Matson, B. D.; Mayer, J. M. *J. Am. Chem. Soc.* **2012**, *134*, 5444. (j) Mase, K.; Ohkubo, K.; Fukuzumi, S. *J. Am. Chem. Soc.* **2013**, *135*, 2800.

(7) (a) Fukuzumi, S. *Prog. Inorg. Chem.* **2009**, *56*, 49. (b) Fukuzumi, S. *Bull. Chem. Soc. Jpn.* **1997**, *70*, 1. (c) Fukuzumi, S.; Ohkubo, K. *Coord. Chem. Rev.* **2010**, *254*, 372. (d) Fukuzumi, S. *Chem. Lett.* **2008**, *37*, 808. (e) Fukuzumi, S.; Mochizuki, S.; Tanaka, T. *Inorg. Chem.* **1989**, *28*, 2459. (f) Fukuzumi, S.; Mochizuki, S.; Tanaka, T. *Inorg. Chem.* **1990**, *29*, 653. (g) Fukuzumi, S.; Mochizuki, S.; Tanaka, T. *J. Chem. Soc., Chem. Commun.* **1989**, 391. (h) Fukuzumi, S.; Okamoto, K.; Gros, C. P.; Guilard, R. *J. Am. Chem. Soc.* **2004**, *126*, 10441. (i) Fukuzumi, S.; Okamoto, K.; Tokuda, Y.; Gros, C. P.; Guilard, R. *J. Am. Chem. Soc.* **2004**, *126*, 17059. (j) Halime, Z.; Kotani, H.; Li, Y.; Fukuzumi, S.; Karlin, K. D. *Proc. Natl. Acad. Sci. U.S.A.* **2011**, *108*, 13990. (k) Peljo, P.; Murtomäki, L.; Kallio, T.; Xu, H.-J.; Meyer, M.; Gros, C. P.; Barbe, J.-M.; Girault, H. H.; Laasonen, K.; Kontturi, K. *J. Am. Chem. Soc.* **2012**, *134*, 5974. (l) Su, B.; Hatay, I.; Troja´nek, A.; Samec, Z.; Khoury, T.; Gros, C. P.; Barbe, J.-M.; Daina, A.; Carrupt, P.-A.; Girault, H. H. *J. Am. Chem. Soc.* **2010**, *132*, 2655. (m) Hatay, I.; Su, B.; Li, F.; Me´ndez, M. A.; Khoury, T.; Gros, C. P.; Barbe, J.-M.; Ersoz, M.; Samec, Z.; Girault, H. H. *J. Am. Chem. Soc.* **2009**, *131*, 13453. (n) Devoille, A. M. J.; Love, J. B. *Dalton Trans.* **2012**, *41*, 65. (o) Askarizadeh, E.; Yaghoob, S. B.; Boghaei, D. M.; Slawinc, A. M. Z.; Love, J. B. *Chem. Commun.* **2010**, *46*, 710.

(8) Kundu, S.; Matito, E.; Walleck, S.; Pfaff, F. F.; Heims, F.; Rabay,´ B.; Luis, J. M.; Company, A.; Braun, B.; Glaser, T.; Ray, K. *Chem. Eur. J.* **2012**, *18*, 2787.

(9) (a) Chandrasekhar, V.; Nagendran, S.; Bansal, S.; Kozee, M. A.; Powell, D. R. *Angew. Chem., Int. Ed.* **2000**, *39*, 1833. (b) Holmes, R. R.; Schmid, C. G.; Chandrasekhar, V.; Day, R. O.; Holmes, J. M. *J. Am. Chem. Soc.* **1987**, *109*, 1408.

(10). (a) Pfaff, F. F.; Kundu, S.; Risch, M.; Pandian, S.; Heims, F.; Pryjomska-Ray, I.; Haack, P.; Metzinger, R.; Bill, E.; Dau, H.; Comba, P.; Ray, K. *Angew. Chem., Int. Ed.* **2011**, *50*, 1711. (b) Wang, B.; Lee, Y.-M.; Tcho, W.-Y.; Tussupbayev, S.; Kim, S.-T.; Kim. Y.; Seo, M. S.; Cho, K. –B.; Dede, Y.; Keegan, B. C.; Ogura, T.; Kim, S. H.; Ohta, T.; Baik, M.-H.; Ray, K.; Shearer, J.; Nam, W. *Nat. Commun.* **2017**, *8*, 14839. (c) Benelli, C.; Gatteschi, D. *Inorg. Chem.* **1982**, *21*, 1788. (d) Fukui, K.; Ohya-Nishiguchi, H.; Hirota, N.; Aoyagi, K.; Ogoshi, H. *Chem. Phys. Lett.* **1987**, *140*, 15.

(11). (a) Stephens, P. J. *Adv. Chem. Phys.* **1976**, *35*, 197. (b). Lehnert, N.; George, S. D.; Solomon, E. I. *Curr. Opin. Chem. Biol.* **2001**, *5*, 176. (c). Solomon, E. I.; Pavel, E. G.; Loeb, K. E.; Campochiaro, C. *Coord. Chem. Rev.* **1995**, *144*, 369-460. (d). Neese, F.; Solomon, E. I. *Inorg. Chem.* **1999**, *38*, 1847. (e). Paulat, F.; Lehnert, N. *Inorg. Chem.* **2008**, *47*, 4963.

(12) a) Lee, C.; Yang, W.; Parr, R. G. Phys. Rev. B 1988, 37, 785. b) Schaefer, A.; Horn, H.; Ahlrichs, R. J. J. Chem. Phys. 1992, 97, 2571. c) Schaefer, A.; Huber, C.; Ahlrichs, R. J. Chem. Phys. 1994, 100, 5829.

(13) Neese, F.; Wennmohs, F.; Becker, U.; Bykov, D.; Ganyushin, D.; Hansen, A.; Izsák, R.; Liakos, D.A.; Kollmar, C.; Kossmann, S.; Pantais, D.A.; Petrenko, T.; Reimann, C.; Riplinger, C.; Roemelt, M.; Sandhöfer, B.; Schapiro, I.; Sivalingam, K.; Wezisla, B. ORCA version 3.0 quantum computing package, Max-Planck Institue for Chemical Energy Conversion, Mülheim an der Ruhr, Germany

(14) Adamsky, H. AOMX program. Heinrich-Heine-Universität, Dusseldorf, **1996**.

(15) (a) Fukuzumi, S.; Tahsini, L.; Lee, Y.-M.; Ohkubo, K.;Nam, W.; Karlin, K. D. *J. Am. Chem. Soc.* **2012,** *134,* 7025.

(16) (a) Givaja, G.; Volpe, M.; Edwards, M. A.; Blake, A. J. Wilson, C.; Schröder, M.; Love, J. B. *Angew. Chem., Int. Ed.* **2007**, *46*, 584. (b) Tanase, T.; Onaka, T.; Nakagoshi, M.; Kinoshita, I.; Shibata, K.; Doe, M.; Fujii, J.; Yano, S. *Chem. Commun.* **1997**, 2115. (c) Askarizadeh, E.; Yaghoob, S. B.; Boghaei, D. M.; Slawin, A. M. Z.; Love, J. B. *Chem. Commun.* **2010**, *46*, 710.

(17) (a) Cho, J.; Sarangi, R.; Kang, H. Y.; Lee, J. Y.; Kubo, M.; Ogura, T.; Solomon, E. I.; Nam, W. *J. Am. Chem. Soc.* **2010**, *132*, 16977. (b) Hu, X.; Castro-Rodriguez, I.; Meyer, K. *J. Am. Chem. Soc.* **2004**, *126*, 13464. (c) Cho, J.; Sarangi, R.; Nam, W. *Acc. Chem. Res.* **2012**, *45*, 1321.

(18) Hopmann, K. H.; Noodleman, L.; Ghosh, A. *Chem. Eur. J.* **2010**, *16*, 10397.